1 Quantifying the seasonal variations and regional transport of PM$_{2.5}$
2 in the Yangtze River Delta region, China: Characteristics, sources,
3 and health risks

4 Yangzhihao Zhan[a], Min Xie[a], Tijian Wang[a], Pulong Chen[b], Jun Tian[c], Kuanguang Zhu[d], Yi Luo[a], Runqi
5 Zhao[a],Shu Li[a], Bingliang Zhuang[a], Mengmeng Li[a]

6 [a] School of Atmospheric Sciences, Nanjing University, Nanjing 210023, China
7 [b] Net Zero Era (Jiangsu) Environmental Technology Co., Nanjing 210023, China
8 [c] Academy of Environmental Planning and Design. Co.,Ltd., Nanjing University, Nanjing 210023, China
9 [d] Hubei Provincial Academy of Eco-Environmental Sciences, Wuhan 430073, China

10 *Correspondence to*: Min Xie (minxie@nju.edu.cn)

11 **Abstract.** Given the increasing complexity of the chemical composition of PM$_{2.5}$, identifying and quantitatively assessing
12 the contributions of pollution sources has played an important role in formulating policies to control particle pollution. This
13 study provides a comprehensive assessment between PM$_{2.5}$ chemical characteristics, sources, and health risks based on
14 sampling data conducted over one year (March 2018 to February 2019) in Nanjing. Results show that PM$_{2.5}$ exhibits a
15 distinct variation across different seasons, which is primarily driven by emissions, meteorological conditions, and chemical
16 conversion of gaseous pollutants. First, the chemical mass reconstruction shows that secondary inorganic aerosols (SIA,
17 62.5 %) and carbonaceous aerosols (21.3%) contributed most to the PM$_{2.5}$ mass. The increasing oxidation rates of SO$_2$ and
18 NO$_2$ from summer to winter indicate that the secondary transformation of gaseous pollutants is strongly positively correlated
19 with relative humidity. Second, the positive matrix factorization (PMF) method shows that identified PM$_{2.5}$ sources include
20 SIA (42.5%), coal combustion (CC, 22.4%), industry source (IS, 17.3%), vehicle emission (VE, 10.7%), fugitive dust (FD,
21 5.8%) and other sources (1.3%). The Hybrid Single Particle Lagrangian Integrated Trajectory (HYSPLIT) model and the
22 concentration-weighted trajectory (CWT) analysis are used to further explore different spatial distributions and regional
23 transport of sources. High emissions (10-11 μg·m^{-3}) of SIA and CC distribute in Nanjing and central China in winter.
24 Moderate emissions (8-9 μg·m^{-3}) of IS and VE are potentially located in the north of Jiangsu, Anhui, and Jiangxi. The PM$_{2.5}$
25 pollution from long-range transport is attenuated by meteorological conditions and ocean air masses. Finally, the health risk
26 assessment indicates that the carcinogenic and non-carcinogenic risks of toxic elements (Cr, As, Ni, Mn, V, and Pb) mainly
27 come from IS, VE, and CC, which are within the tolerance or acceptable level. Although the main source of pollution in
28 Nanjing is SIA at present, we should pay more attention to the health burden of vehicle emissions, coal combustion, and
29 industrial processes.

30 **1. Introduction**

31    $PM_{2.5}$ is particulate matter with an aerodynamic equivalent diameter less than or equal to 2.5 μm, and one of the most
32   important air pollutants, which can affect air quality (Sharma et al., 2020), atmospheric visibility (Tseng et al., 2019) and
33   ecosystems (Li et al., 2021). $PM_{2.5}$ can directly enter the human body through the respiratory system and lead to increased
34   health risks (Kumar et al., 2019; Sulaymon et al., 2021). $PM_{2.5}$ concentrations in the United States and Europe have begun to
35   decrease since the 1980s, and those in Japan gradually decreased after 2012 (Zhang et al., 2020). In China, the annual
36   average concentration of $PM_{2.5}$ has decreased by 50% with the implementation of the Air Pollution Prevention and Control
37   Action Plan (APPCAP) in 2013 (Zeng et al., 2019). However, $PM_{2.5}$ pollution levels remain higher than the World Health
38   Organization recommendation (35 μg·m^{-3}), and the number of deaths caused by $PM_{2.5}$ exceeds one million per year (Zhu et
39   al., 2020). It indicates that a comprehensive assessment between $PM_{2.5}$ chemical characteristics, sources, and health risks is
40   significant for pollution control measures in the key regions of China.

41   Understanding the chemical composition of $PM_{2.5}$ is important for formulating control strategies. Sulfate, nitrate, and
42   ammonium (SNA) are the major secondary inorganic aerosols, whose chemical conversion occurs in homogeneous and
43   heterogeneous reactions (Fan et al., 2020; Chow et al., 2022). Variations in the form of SO_4^{2-} and NH_3 lead to variations in
44   the acid-base balance of aerosols (Roper et al., 2019). The organic carbon (OC) and elemental carbon (EC) in $PM_{2.5}$ are
45   mainly derived from thousands of organic compounds and primary sources of combustion products (Wu et al., 2020). Both
46   NO_3^-/SO_4^{2-} and OC/EC ratios can be reasonably used to evaluate the contribution of mobile and stationary sources to $PM_{2.5}$
47   in the atmosphere (Zhan et al., 2021). To identify the sources of $PM_{2.5}$, receptor modelings have been developed, which
48   include positive matrix factorization (PMF), chemical mass balance (CMB), and principal component analysis (PCA) (Zong
49   et al., 2016; Lv et al., 2020). Recently, the combination of the PMF model and trajectory modeling has proven to be
50   powerful to identify source regions and quantify chemical compositions for a receptor site (Zheng et al., 2019). In addition,
51   the health risks of air exposure through the inhalation of $PM_{2.5}$ are beyond acceptable levels (Jiang et al., 2018; Xie et al.,
52   2020). Air exposure models have been widely used to further assess the non-carcinogenic and carcinogenic health risks of
53   toxic elements in $PM_{2.5}$ (Behrooz et al., 2021; Fang et al., 2021; Li et al., 2022).

54   Chemical characteristics of $PM_{2.5}$ have been widely investigated in the Beijing-Tianjin-Hebei (BTH), the Yangtze River
55   Delta (YRD), and the Pearl River Delta (PRD) during the last decade (Huang et al., 2017; Liu et al., 2017; Sun et al., 2020).
56   Source apportionment studies mainly focus on the relative importance of local emission and regional transportation on $PM_{2.5}$
57   at a specific site using the PMF model and the backward trajectory analysis (Zheng et al., 2019; Yan et al., 2021; Lv et al.,
58   2022). Compared with other methods, the PMF model can provide both the source profiles and contributions of various
59   sources as a model outcome (Li et al., 2020). Some studies involved the health risks of toxic elements in $PM_{2.5}$ (Zhang et al.,
60   2019; Fang et al., 2021), and only a few studies discussed the classification of toxic elements according to PMF results
61   (Wang et al., 2019; Wang et al., 2020). However, there were two shortcomings in previous studies: (1) Given the uneven
62   geographical distribution of observation sites and difficulties in data collection, most studies were based on short-term data
63   comparisons and lacked systematic comparisons of the distinctive seasonality, regional transport, and meteorological effects

64 of various elements and sources. (2) A comprehensive assessment of the health risks of toxic elements in each source of

65 PM$_{2.5}$ was still scarce, which limited the implementation of long-term pollution control measures in megacities.

66   The YRD region is China's scientific research base and comprehensive transportation hub. The annual PM$_{2.5}$

67 concentration in the YRD has been reduced by 45.6% from 2016 to 2018. However, as a mega-city in the YRD, the PM$_{2.5}$ in

68 Nanjing still exceeds the National Ambient Air Quality Standard (35 μg·m^{-3} as an annual average) by more than 38 % (Nie

69 et al., 2018). In this work, we provide high-quality composition data for PM$_{2.5}$ in the typical YRD city, including their

70 chemical characteristics and diurnal variations. Besides, the measured PM$_{2.5}$ in its entirety is successfully apportioned to

71 various contributing sources by PMF and CWT methods. Finally, potential risks associated with exposure to airborne toxic

72 elements are identified based on the health risk assessment. The results can systematically assess the relationship between

73 chemical characteristics, sources, and health risks of PM$_{2.5}$, and serve to guide PM$_{2.5}$ control measures for other megacities.

74 **2. Data and Methodology**

75 **2.1 Chemical component sampling, air quality and meteorological data**

76   Hourly concentrations of particulate matter (PM) components from December 2018 to February 2019 in Nanjing were

77 used in this study. The elemental carbon (EC), organic carbon (OC), 30 trace elements (Si, Al, As, Ca, K, Co, Mo, Ag, Sc, Tl,

78 Pd, Br, Te, Ga, Cs, Pb, Se, Hg, Cr, Cd, Zn, Cu, Ni, Fe, Mn, Ti, Sb, Sn, and V) and the 8 inorganic components in aerosols

79 (Na$^+$, K$^+$, Mg^{2+}, Ca^{2+}, Cl$^-$, NO$_3^-$, SO$_4^{2-}$, and NH$_4^+$) were quantified in each PM$_{2.5}$ sample. PM$_{2.5}$ samples were collected on

80 the rooftop of the School of Atmospheric Sciences, Xianlin Campus, Nanjing University (32.12 °N, 118.96 °E). OC and EC

81 were analyzed by the online carbon fraction Monitor (EA-32, Everisetech Co., Beijing). OC and EC were separated by step

82 heating and then determined by the non-dispersive infrared method. The components of heavy metals were collected by the

83 atmospheric heavy metal Monitor (AMS-100, Fpigroup Co., Hangzhou). The volumetric concentration of heavy elements

84 (ng·m^{-3}) was obtained by detecting the concentration of PM enriched on the filter membrane using the β ray absorption

85 principle (Wang et al., 2020). The inorganic components sampling instrument was the In-situ Gas and Aerosol Compositions

86 Monitor (IGAC, Fortelice International Co., Taiwan). It consisted of the wet concentric circular tube, the gas gel processor,

87 and the ion chromatograph. The sampling inlet was about 20 m above the ground and the flow rate was 16.67 L·min^{-1}. The

88 collected liquid samples were filtered by defoaming and then injected into the ion chromatography analyzers to analyze the

89 ion components from the gases and the aerosols.

90   Air pollutants, including PM$_{2.5}$, PM$_{10}$, O$_3$, NO$_2$, SO$_2$, and CO, were monitored by the National Environmental

91 Monitoring Center (NEMC) of China. These data were issued hourly on the national urban air quality real-time publishing

92 platform (https://air.cnemc.cn:18007/, last access: 7 April 2023). The detection limits were below 0.12 μg·m^{-3} and the

93 collection efficiency was higher than 90% (Zhan et al., 2021). Meteorological parameters included air pressure, air

94 temperature, relative humidity, wind speed, and boundary layer height. We collected hourly data from the National Climatic

95 Data Center (NCDC) of the University of Wyoming website (http://weather.uwyo.edu/surface/, last access: 7 April 2023).

96 Regarding boundary layer height, daily sounding vertical profiles were extracted from the national benchmark climate

97 Nanjing station 58238 (32.00 °N, 118.48 °E) and were also acquired from this website. The quality assurance and quality

98 control (QA/QC) procedures were used at each site according to the method of Xie et al. (2016) and Gao et al. (2021). In this

99 study, we defined the blank sampling of atmospheric pollutant data as -999 to facilitate PMF processing. The chemical mass

100 reconstruction method was used to correct potential measurement errors, which was described in detail in Section 2.2. The

101 QA/QC procedures have passed the artificial random inspection of extreme value and time consistency.

102 **2.2 Mass and chemical composition determination for PM$_{2.5}$**

103 Due to the limitation in sampling location and equipment, the sum of measured species was often lower than the

104 gravimetric mass. Chemical mass reconstruction (CMR) attempted to achieve closure between the gravitational mass and the

105 sum of components and correct potential measurement errors. In this study, the reconstructed result and the gravimetric

106 result exhibited a significant correlation, with a mean R^2 of 0.93, indicating that the chemical reconstruction method had

107 strong reliability. Following the work of Xu et al. (2021), eight categories of chemical components in chemically

108 reconstructed PM$_{2.5}$ can be expressed as follows:

109 $$PM_{2.5} = OM + EC + MD + TM + SO_4^{2-} + NO_3^- + NH_4^+ + Cl^- \tag{1}$$

110 where OM refers to the organic matter. The OC to OM conversion coefficient at urban sites is 1.6 (Brokamp et al., 2017).

111 The calculation of mineral dust (MD) is based on crustal element oxides (Yan et al., 2020):

112 $$MD = 2.14 \times Si + 1.67 \times Ti + 1.89 \times Al + 1.40 \times Ca + 1.58 \times Mn + 1.43 \times Fe + 1.21 \times K + 1.67 \times Mg \tag{2}$$

113 where Si is estimated as multiplying Al in crustal material by a converting factor (3.14) (Zheng et al., 2019). Trace metals

114 (TM) represent the sum of 30 different types of heavy metals:

115 $$\begin{aligned} TM = &As + Co + Mo + Ag + Sc + Tl + Pd + Br + Te + Ga + Cs + Pb \\ &+ Se + Hg + Cr + Cd + Zn + Cu + Ni + Sb + Sn + V + Ba \end{aligned} \tag{3}$$

116 **2.3 Identification of source by the positive matrix factorization (PMF) model**

117 The positive matrix factorization (PMF) was developed by the Environmental Protection Agency (EPA) and has been

118 widely adopted to classify PM$_{2.5}$ into different factors (Zong et al., 2016). The basic principle of the PMF model was to

119 calculate the weight error of each chemical component in the particulate matter and then determined its main pollution

120 source and contribution rate by the least square method (Paatero and Tapper, 1994). The equation of the PMF model can be

121 expressed as follow:

122 $$X_{ij} = \sum_{k=1}^{p} g_{ik} f_{kj} + e_{ij} \tag{4}$$

123 where X_{ij} is the concentration of the ijth sample; g_{ik} represents the contribution of the ikth sample; f_{kj} represents the

124 mass fraction of the jkth and e_{ij} is the residual between the measured mass concentration of the ijth sample and its analytical

125 value. The purpose of the PMF model is to find the minimum Q value with the concentration file and uncertainty file (u_{ij})

126 introduced into the model. The objective function Q is defined as follows:

$$Q_{ij} = \sum_{i=1}^{n} \sum_{j=1}^{m} \left[\frac{X_{ij} - \sum_{k=1}^{p} g_{ik} f_{kj}}{u_{ij}} \right]^2 \qquad (5)$$

128 where Q is the sum of all sample residuals and their uncertainties u. In this study, the fitting species included 41 types of

129 chemical species of PM$_{2.5}$ that were selected and validated to ensure that the value of the objective function Q was

130 minimized.

131 First, we excluded more than 50% of the dataset for species below the method detection limit (MDL) and retained 23

132 species that were significantly correlated with PM$_{2.5}$. Second, we calculated the uncertainty (Unc) for each species based on

133 the concentration fraction and MDL (Taylor et al., 2020). Third, different numbers of factors were tested with random seeds

134 in 20 iterations of each run. When the number of factors was set to six, the fitting degree of the model calculation results was

135 the highest, with a correlation coefficient of 0.93, and the species almost showed a normal curve. Finally, the bootstrap (BS)

136 and displacement (DISP), and BS-DISP diagnostic analysis were also used to evaluate the rationality of the apportioned

137 factor profiles and contributions. BS is used to detect and estimate the disproportionate effects of a small set of observations

138 on the solution and also, to a lesser extent, the effects of rotational ambiguity. The value of the F-peak strength was ensured

139 to be 0.5 to eliminate the rotation ambiguity. The mapping for each factor in this study was more than 80% from the BS run,

140 indicating the six-factor solution was appropriate.

141 **2.4 Source apportionment by backward trajectory calculation and CWT analysis**

142 The Hybrid Single Particle Lagrangian Integrated Trajectory (HYSPLIT) model was developed by the National

143 Oceanic and Atmospheric Administration (NOAA) and the Bureau of Meteorology Australia to simulate and analyze the

144 movement, deposition, and diffusion of airflow. The reanalysis data with a spatial resolution of one degree and a temporal

145 resolution of 6 h (00:00, 06:00, 12:00, and 18:00 UTC) were obtained from the Global Data Assimilation System (GDAS)

146 (https://rda.ucar.edu/datasets/, last access: 7 April 2023).. To locate the potential source areas for the corresponding

147 components, we used the HYSPLIT model to analyze the backward trajectory of airflow from March 2018 to February 2019.

148 48-hour backward trajectories terminated at a height of 100 m above ground level were calculated at the starting point

149 (32.07 °N, 118.78 °E). Due to the high uncertainty of a single backward trajectory, we drew multiple trajectories and

150 performed cluster analysis. The cluster analysis was a multivariate statistical technique using the Angle Distance algorithm,

151 which could quantify the relationship among the pollution concentrations in each source area (Shu et al., 2017).

152 The concentration-weighted trajectory (CWT) analysis was further used to determine the relative contribution of

153 different areas. The CWT analysis was conducted by the TrajStat software, which was a GIS (geographic information system)

154 application that enabled the user to visualize and analyze the spatial and meteorological data with multiple data formats

155 (Feng et al., 2021). In this study, the meteorological data used for the HYSPLIT model and the CWT method remained the

156 same. The CWT method divided the research area into small equal grids, set a standard value for the research object, and

157 defined the trajectory exceeding the standard value as the pollution trajectory. The spatial resolution was 0.5×0.5 (Liu et al.,

158 2018). The CWT method reflected the pollution degree of different trajectories by calculating the weight concentration of the

159 airflow trajectory in potential source areas:

160 $$C_{ij} = \frac{1}{\sum\limits_{i=1}^{M} \tau_{ijl}} \sum\limits_{l=1}^{M} C_l \tau_{ijl} \qquad (6)$$

161 where C_{ij} is the average weight concentration of grid ij , C_l is the pollutant concentration based on trajectory l that passes

162 through grid ij , and τ_{ij} is the residence time of trajectory l in grid ij . Similarly, to reduce the uncertainty caused by the

163 smaller n_{ij} , the CWT value is multiplied by the weight function as well (Wong et al., 2022):

164 $$W_{ij} = \begin{cases} 1.00 & \left(80 < n_{ij}\right) \\ 0.72 & \left(20 < n_{ij} \le 80\right) \\ 0.42 & \left(10 < n_{ij} \le 20\right) \\ 0.05 & \left(n_{ij} \le 100\right) \end{cases} \qquad (7)$$

165 where n_{ij} is the number of trajectories that pass through the ij^{th} cell. W_{ij} is an empirical weight function to reduce the undue

166 influence of small n_{ij} on the CWT values (Fan et al., 2019). In this study, the CWT value of each identified source derived

167 from the PMF model was calculated.

168 **2.5 Health risk assessment**

169   The human health risk from heavy metals in PM$_{2.5}$ may occur through exposure to ambient air (Zhang et al., 2019).

170 Based on the PMF analysis, we selected six toxic elements (Cr, As, Ni, Mn, V, and Pb) for the exposure risk assessment. Cr,

171 Ni and As have both carcinogenic and non-carcinogenic effects, Mn and V mainly have non-carcinogenic effects, and Pb

172 mainly produces a carcinogenic effect (Jiang et al., 2018). The non-carcinogenic and carcinogenic risks from the toxic

173 species of PM$_{2.5}$ were evaluated by the hazard quotient (HQ) and lifetime carcinogenic risk (LCR), respectively. The US

174 EPA human health risk assessment models were used to conduct carcinogenic and non-carcinogenic risk assessments (Khan

175 et al., 2016):

176 $$EC_{inh} = \frac{GA \times ET \times EF \times ED}{AT} \qquad (8)$$

177 $$HQ = \frac{EC_{inh}}{RfC_i \times 1000 \mu g \cdot mg^{-1}} \qquad (9)$$

178 $$LCR = IUR \times EC_{inh} \qquad\qquad (10)$$

179 where EC_{inh} is the average daily exposure concentration of toxic elements inhaled through respiration. GA is the

180 concentration of toxic elements in each source composition. ET, EF, ED and AT are the exposure time, exposure

181 frequency, exposure duration and average exposure time, respectively. RfC_i is the inhalation reference concentration

182 (mg·m⁻3). IUR is the inhalation unit risk($(\mu g \cdot m^{-3})^{-1}$). HQ greater than 1 indicated a non-carcinogenic risk to human health.

183 For carcinogenic risk, LCR < 10^{-6} means no cancer risk, LCR between 10^{-6} and 10^{-4} is acceptable or tolerable, and LCR > 10^{-4}

184 is intolerable. The exposure parameters were shown in Table 1 (Jiang et al., 2018; Zhang et al., 2019).

185 **Table 1. Exposure parameters of toxic elements through inhalation route in health risk assessments.**

Toxic elements	RfC$_i$ (μg·m⁻³)⁻¹	IUR (mg·m⁻³)
Cr	1.0×10^{-4}	1.2×10^{-2}
As	1.5×10^{-5}	4.3×10^{-3}
Ni	1.4×10^{-5}	2.4×10^{-4}
Mn	5.0×10^{-5}	——
V	1.0×10^{-4}	——
Pb	——	1.2×10^{-5}

186 ## 3. Results and discussions

187 ### 3.1 Chemical components, meteorological parameters and diurnal variations

188   Table 2 shows the seasonal average of chemical components and meteorological parameters from March 2018 to

189 February 2019. In this study, March to May 2018 is defined as spring, June to August 2018 is defined as summer, September

190 to November 2018 is defined as fall, and December 2018 to February 2019 is defined as winter. The concentration of PM$_{2.5}$

191 ranged from 6.7 to 234.0 μg·m⁻³, with an annual average of 68.7 μg·m⁻³. The order of average concentrations of PM$_{2.5}$ in

192 each season was winter (113.9 μg·m⁻³) > spring (99.1 μg·m⁻³) > autumn (38.9 μg·m⁻³) > summer (23.7 μg·m⁻³). Seasonal

193 variations of PM$_{2.5}$ were closely related to meteorological conditions. In spring, the wind speed (WS) was higher in spring

194 (3.5 m·s⁻¹) than those in other seasons. Pearson correlation showed that PM$_{2.5}$ concentrations were significantly (p<0.01)

195 correlated to WS (r=-0.36) in spring. In summer, high boundary layer height (BLH) (520.4m) significantly reduced PM$_{2.5}$

196 concentrations. In autumn and winter, PM$_{2.5}$ showed significant correlations between temperature (r=-0.53) and relative

197 humidity (r=0.62). High humidity (79.6%) and low temperature (4.9°C) in winter promoted the accumulation of pollutants.

198   The seasonal variation of anthropogenic emissions also considerably affected PM$_{2.5}$ concentrations. The order of the

199 major components in PM$_{2.5}$ was NO$_3^-$ (20-31%) > SO$_4^{2-}$ (16-27%) > NH$_4^+$ (11-19%) > mineral dust (8-14%) > OM (6-

200 14%) > EC (2-4%) > trace metals (2-3%) > Cl⁻ (1-3%). Sulfate, nitrate, and ammonium (SNA) accounted for 60% of the

201 total PM$_{2.5}$ and were closely related to the secondary transformation of gaseous precursors. The concentration ratio of NO$_3^-$
202 to SO$_4^{2-}$ (NO$_3^-$/SO$_4^{2-}$) was used to differentiate the relative importance of nitrogen (generally affected by vehicles) and
203 sulfur (normally affected by stationary sources) in the atmosphere (Liu et al., 2019). Over the past few years, the mass ratio
204 of NO$_3^-$/SO$_4^{2-}$ was 2.13 in Ningbo, 1.89 in Hangzhou, and 1.21 in Beijing (Huang et al., 2017; Wang et al., 2018). In this
205 study, the average ratios of NO$_3^-$/SO$_4^{2-}$ in the four seasons were 1.81, 1.20, 2.34, and 1.59, indicating that the contribution of
206 mobile sources was greater than that of stationary sources throughout the year. Carbonaceous aerosols (OM and EC)
207 accounted for 12% and 14% in spring and winter. The large increase in the number of coal fires used for residential heating
208 in winter may increase the abundance of carbon-containing emissions, including OC, EC, and VOC$_S$ (Islam et al., 2020).
209 Compared with 2015, the concentrations of OM and EC decreased from 22.9% to 12.8% (Chen et al., 2017). This may be
210 related to policies to control coal combustion and motor vehicle emissions, considering similar meteorological conditions in
211 the two periods.

212 **Table 2. Average of components of PM$_{2.5}$ and meteorological parameters in each season (μg·m^{-3}). T, RH, WS, and BLH represent**
213 **air temperature, relative humidity, wind speed and boundary layer height, respectively.**

Average concentrations: μg·m^{-3} (component percentages: %)	Spring	Summer	Autumn	Winter
PM$_{2.5}$	99.1	23.7	38.9	113.9
SO$_4^{2-}$	20.5 (20.7)	5.2 (21.9)	7.3 (18.8)	31.5 (27.7)
NO$_3^-$	16.9 (17.1)	5.3 (22.4)	9.8 (25.2)	27.2 (23.9)
NH$_4^+$	15.1 (15.2)	3.2 (13.5)	7.1 (18.3)	11.5 (10.1)
OM	11.7 (11.8)	1.6 (6.8)	4.1 (10.5)	11.0 (9.7)
EC	2.3 (2.3)	0.8 (3.4)	1.6 (4.1)	3.6 (3.2)
Mineral dust	13.2 (13.3)	2.3 (9.7)	2.7 (6.9)	8.7 (7.6)
Trace metals	2.7 (2.7)	0.5 (2.1)	0.5 (1.3)	1.6 (1.4)
Cl$^-$	2.7 (2.7)	1.6 (6.8)	0.8 (2.1)	1.7 (1.5)
T (°C)	18.8	27.6	19.4	4.9
RH (%)	86.5	58.2	73.1	79.6
WS (m·s^{-1})	3.5	2.9	2.7	2.1
BLH (m)	469.7	520.4	443.6	419.7

214 Figure 1 shows the diurnal variation of chemical components in PM$_{2.5}$. The seasonal differences were mainly reflected
215 in the variation in the timing of peak values. The lowest PM$_{2.5}$ concentrations were 94.8 μg·m^{-3} at 17:00 in spring and 120.3
216 μg·m^{-3} at 14:00 in winter, which were related to the meteorological conditions. In spring (Fig. 1a), the concentration of SNA
217 had obvious diurnal variations. From 6:00 to 18:00, the average concentration of NO$_3^-$ increased from 17.6 to 21.8 μg·m^{-3},

218   while the average concentration of SO_4^{2-} decreased from 23.2 to 15.9 μg·m^{-3}. In summer (Fig. 1b), the highest and lowest

219   pollution concentrations were 23.5 μg·m^{-3} at 9:00 and 14.2 μg·m^{-3} at 14:00, respectively. The maximum difference in

220   concentration between day and night was less than 10 μg·m^{-3}, indicating the study area was in a relatively stable background

221   field. Generally, high humidity, low wind speed, and low temperature tend to promote the secondary transformation of

222   gaseous pollutants (Chen et al., 2018). In addition, the occurrence time of the daily minimum values of PM$_{2.5}$ concentrations

223   in winter was earlier than those in spring. The height of the atmospheric boundary layer decreased early in the winter

224   afternoons due to less solar radiation. As shown in Figure 1d, from 18:00 to 23:00, the concentration of SNA increased from

225   74.5 μg·m^{-3} to 108.7 μg·m^{-3}, with increasing rates of 8.5 μg·m^{-3}·h^{-1}. The values of PM$_{2.5}$ in winter were higher at night due to

226   the coal combustion and biomass burning for residential heating (Zou et al., 2017). In summary, compared with the spring

227   and winter, PM$_{2.5}$ presented similar and relatively flat diurnal patterns in both autumn and summer. Although the seasonal

228   variations of mass concentrations and aerosol compositions were substantially different, the concentrations of aerosol species

229   showed similar diurnal variation patterns during all the sampling days with higher values in the nighttime and early morning,

230   suggesting that the factors driving the diurnal variations were similar.
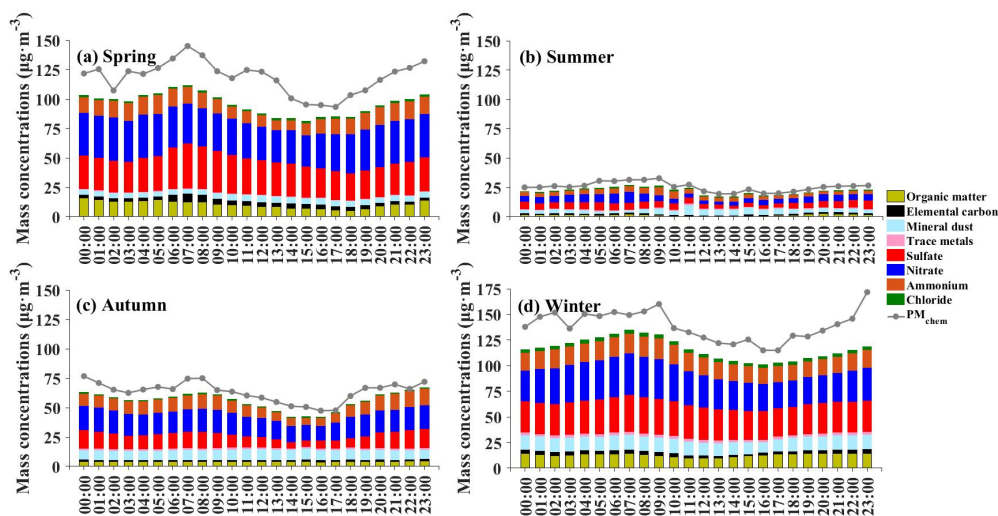
231   **Figure 1. Diurnal variations in the major chemical components of PM$_{2.5}$.**

232   **3.2 Variation of PM$_{2.5}$ chemical compositions at different pollution levels**

233   Figure 2 presents the PM$_{2.5}$ concentrations and components at different pollution levels. In this study, it was defined as

234   the clean day (C) when the daily average PM$_{2.5}$ concentration < 75 μg·m^{-3}, the moderate pollution day (MP) when 75 μg·m^{-3}

235   ≤ PM$_{2.5}$ < 150 μg·m^{-3}, and the heavy pollution day (HP) when PM$_{2.5}$ ≥ 150 μg·m^{-3}. As shown in Figure 3a, the WSIIs were

236   largely responsible for the variability in PM$_{2.5}$. The contributions of SNA in spring and winter were similar, with ratios of

237   65.0% for clean days, 75.0% for moderate pollution days, and 83.9% for heavy pollution days. With the degradation of air

238   quality, the contribution of NO_3^- noticeably increased from 27.5% to 47.8% in spring and from 28.9% to 44.7% in autumn.
239   To understand the oxidation rates of SO_2 and NO_2, the sulfur oxidation rate and nitrogen oxidation rate (defined as SOR =
240   $SO_4^{2-}/(SO_4^{2-}+SO_2)$ and NOR = $NO_3^-/(NO_3^- + NO_2)$)) were calculated. The critical value of SOR and NOR in the atmosphere
241   are both 0.1 (Win et al., 2020). The order of the seasonal average NOR was winter (0.21) > spring (0.18) > autumn (0.17) >
242   summer (0.15), while the order of the seasonal average SOR was winter (0.51) > spring (0.43) > autumn (0.42) > summer
243   (0.36). SOR and NOR showed a strong positive correlation with relative humidity, with a correlation coefficient of 0.53 and
244   0.61, respectively. The increase in relative humidity is conducive to the growth of aerosol moisture absorption and
245   heterogeneous oxidation on the surface of aerosol droplets, which is positively correlated with $PM_{2.5}$ concentrations (Islam et
246   al., 2020). From summer to winter, the NOR and SOR values increased by 40.0% and 41.6%, respectively. Due to the high
247   humidity (79.6%) and low temperature (4.9°C) in winter, meteorological conditions provided favorable conditions for the
248   transformation of gaseous precursors.

249   Coal combustion, biomass burning, and motor vehicle emissions all lead to a remarkable increase in carbonaceous
250   aerosols (Zhou et al., 2017). As shown in Figure 2b, carbonaceous species also had a significantly enhanced contribution in
251   the colder season compared to the warmer season. The differences in different seasons might be related to the effects of
252   meteorological conditions and source emissions. Pearson correlation showed that the relationships between OM and EC and
253   meteorological parameters (T, RH, WS, and BLH) were not significant (Table 2). To explore the possible pollution sources,
254   it is feasible to study the mass ratio of OC/EC under different pollution levels. OC is generally formed by photochemical
255   reactions or emitted directly. EC is mainly derived from combustion processes (Zheng et al., 2019). The OC/EC mass ratio
256   of motor vehicle emissions (1.1) is lower than that of coal combustion (2.7) and biomass burning (9.0) (Xu et al., 2021). In
257   this study, the OC/EC ratios continuously decreased as air pollution got worse, and the values ranged from 6.1 (C), 4.1 (MP)
258   to 3.9 (HP) in spring, from 6.2 (C) to 4.8 (MP) in autumn and from 4.3 (C), 2.7 (MP) to 1.3 (HP) in winter. The annual
259   average ratio of OC/EC decreased by 56.1% from clean days to heavy pollution days. The variation in the OC/EC ratio was
260   mainly due to the change in traffic and coal emission sources.
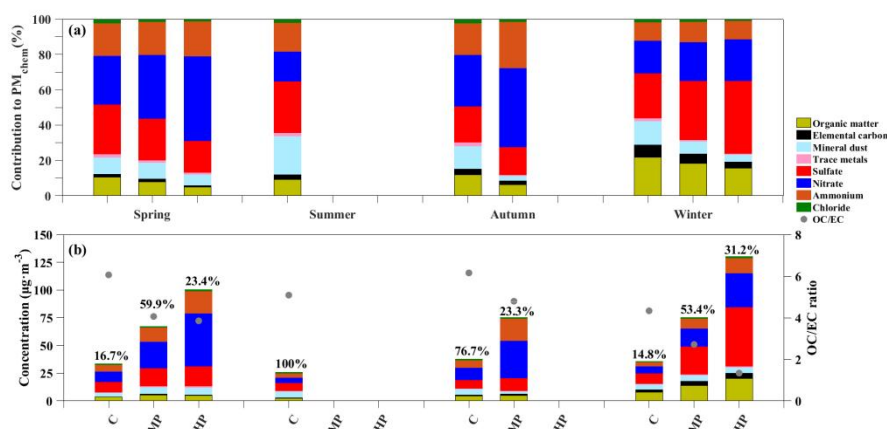
Figure 2. Chemical compositions of PM$_{2.5}$ and mass ratio of OC/EC at different pollution levels. "%" represents the proportion of the filter sample quantity at each pollution level out of the total samples.

3.3 Source identification and apportionment

3.3.1 Elemental profile and source apportionment from the PMF model

To further quantitatively determine the source apportionment of PM$_{2.5}$, the EPA PMF5.0 model was adopted. Figure 3 presents the source profiles and relative contributions of six sources to each species, including secondary inorganic aerosol (SIA), coal combustion (CC), industry source (IS), vehicle emission (VE), fugitive dust (FD), and other sources. As shown in Figure 3a, the compositions of SIA were more clear than other sources. NO$_3^-$ and SO$_4^{2-}$ are mainly from the oxidation of NO$_X$ and SO$_2$, while NH$_4^+$ probably comes from the conversion processes between ammonia and sulfuric and nitric acid (Win et al., 2020). Factor 1 was identified as the SIA with distinctly high loads of NH$_4^+$ (66.9%), NO$_3^-$ (61.9%), SO$_4^{2-}$ (63.8%) and Cl$^-$ (55.3%). In Figure 3b, the high proportion of Pb (38.2%) and Se (45.1%) was identified in Factor 2, associating with moderate weighting on As (14.3%), SO$_4^{2-}$ (20.5%), and Cl$^-$ (22.2%). Pb and As are important identifying elements of coal combustion and are used as tracers (Xie et al., 2020). SO$_4^{2-}$ is formed by the photochemical oxidation of sulfur-containing precursors (SO$_2$ and H$_2$S) released by coal combustion (Zong et al., 2016). Factor 2 was relevant to the CC. In Figure 3c, the compositions with large contributions included heavy metal pollutants such as As (42.8%), Pb(33.8%), Cr (61.1%), Zn (58.9%), Cu (59.4%), Fe (38.3%), and Mn (40.1%). As, Pb, Cr, Fe and Mn are related to metal smelting and processing (Fang et al., 2021). Cu, Zn, and OC are used as tracers of a mixed source of traffic and industrial (Wang et al., 2020). However, OC was the major pollutant in the vehicle exhaust while the contribution of OC was not significant in Figure 3c. Cu and Zn in Figure 3c were mainly from industrial process sources. As discussed above, Factor 3 was attributed to the IS. In figure 3d, the higher proportions of Ni (54.7%), V (80.5%), OC (55.4%), and EC (79.8%) in Factor 4 indicated the source of vehicle emission. OC and EC are mainly from the vehicle exhaust, and Ni and V are generally regarded as tracer elements for engine oil combustion (Wu et al., 2020). In addition, Factor 4 also showed a high loading on NO$_3^-$ (20.3%). The combustion of gasoline and diesel is an important source of NO$_X$ and VOCs, which in turn affects the transformation of NO$_3^-$ from gas to particles (Guevara et al., 2021). In Figure 3e, this factor had relatively high proportions of Fe (31.1%), Ti (78.2%), K$^+$ (55.8%), Ca^{2+} (60.5%), and Mg^{2+} (48.3%). Ti, Fe, and Mg are both common crustal elements that can represent the source of mineral dust. K$^+$ and Ca^{2+} are considered to be significant tracers of biomass burning, which have obvious seasonal variations (Tong et al., 2020; Yan et al., 2020). Factor 5 was classified as the FD, including road dust, industrial dust, and soil dust. Factor 6 (Fig. 3f) was unidentified and could be affected by coal combustion, industrial processes, and biomass burning.
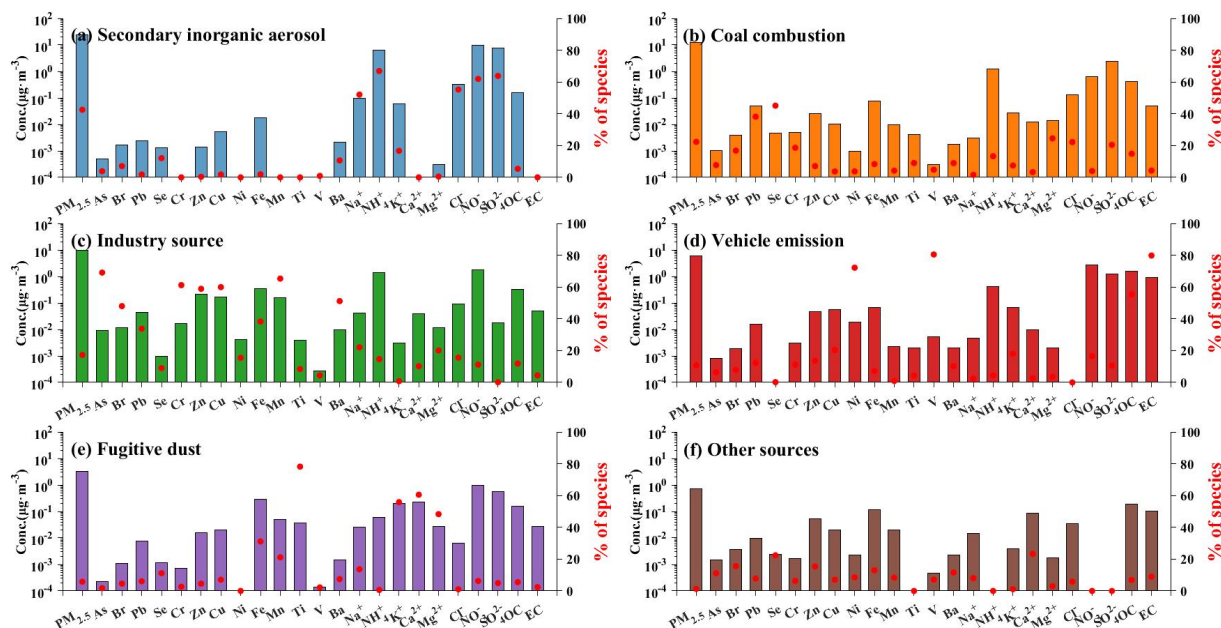
Figure 3. Factor profiles (% of species total) in each source for PM$_{2.5}$. The histograms are the mass concentration of each species to every species, and the red dots are the relative contributions of each source to every species.

Table 3 and Figure 4 show the comparisons of our PMF results with the previous findings. For all studies, the secondary aerosols were the biggest contributor to PM$_{2.5}$ in China from 2014 to 2018. In the YED region, SIA contributed about 42.5% to PM$_{2.5}$ in Nanjing in this study, which was higher than that reported by Sun et al. (2020), while the contributions of CC and IS were lower. However, other sources of PM$_{2.5}$ in different cities were more complicated. In the BTH, IS was crucial source and contributed about 30% of Tianjin and Shijiazhuang (Huang et al., 2017). In contrast, IS in Nanjing contributed only 17.3% of PM$_{2.5}$ pollution. Recent emission control policies in the YRD have had positive effects on reducing industrial pollution. In the PRD, SIA, VE, and biomass burning were identified as the major sources of PM$_{2.5}$. VE showed noteworthy local emission characteristics (Zhou et al., 2017). In this study, CC contributed 22.4% and VE contributed only 10.7% in Nanjing. It is worth noting that the PMF model assumes that source profiles do not change significantly over time and that species do not undergo chemical reactions (Paatero and Tapper, 1994). The human activities under seasonal variations in this study made the actual pollution incompatible with the ideal assumption. For example, emissions from coal combustion in winter increased the contribution of CC significantly in winter (Xu et al., 2021). In addition, the sources of air masses in each season also created uncertainties. All of these required detailed discussions of regional transport conditions in each season.

306   **Table 3. Comparisons of source apportionment among different cities.**

Location		Time	Main pollution sources (proportion)	Investigator
YRD	Nanjing	2018	SIA (42.5%); Coal combustion (22.4%); Industry source (17.3%)	This study
	Nanjing	2015	SIA (37.8%); Coal combustion (27.2%); Vehicle emission (16.4%)	Sun et al. (2020)
	Ningbo	2015	SIA (27.6%); Vehicle emission (18.7%); Industry source (19.4%)	Wang et al. (2018)
BTH	Beijing	2017	SIA (35.6%); Coal combustion (30.8%); Biomass burning (12.5%)	Xu et al. (2021)
	Tianjin	2014	SIA (29.2%); Industry source (25.9%); Vehicle emission (15.7%)	Huang et al. (2017)
	Shijiazhuang	2014	SIA (36.4%); Industry source (29.3%); Vehicle emission (17.9%);	Huang et al. (2017)
PRD	Hong Kong	2015	SIA (49.9%); Industry source (13.5%); Biomass burning (10.8%)	Chow et al. (2022)
	Shenzhen	2014	SIA (30.0%); Vehicle emission (21.6%); Biomass burning (11.5%)	Zhou et al. (2017)
	Guangzhou	2014	SIA (34.6%); Vehicle emission (28.6%); Biomass burning (23.1%)	Li et al. (2020)
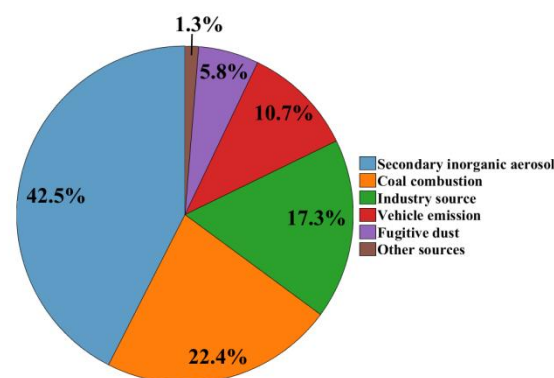
307   **Figure 4. The annual contribution of each source to PM2.5.**

308   **3.3.2 Source identification by backward air mass trajectory analysis**

309   The regional transport of air pollutants exerts a profound impact on local air quality (Shu et al., 2017). Figure 5 shows

310   the quantified contributions of $PM_{2.5}$ with 48-h backward trajectories. In spring (Fig 5a), nearly half of the air masses (cluster

311   a3) stemmed from northern Jiangxi, passed over Anhui Province before arriving at the sampling sites, and had the highest

312    $PM_{2.5}$ average value (127.2 $\mu g \cdot m^{-3}$). CC from cluster a3 had the highest contribution with mass and percentage contributions

313   being 41.0 $\mu g \cdot m^{-3}$ and 32.3%, respectively. Considering that the largest coal-fired thermal power plant in Jiangxi was located

314   in the northern city of Jiujiang (Wang et al., 2018) and there were many industrial cities located along this pathway, regional

315   transport from these areas would have a potentially high impact on the formation of severe particle pollution in Nanjing. In

316   summer (Fig 5b), the most obvious characteristic of regional transport was significantly influenced by the ocean. Clusters b2

317   and b3 were relatively clean with low concentrations of $PM_{2.5}$ (28.2 $\mu g \cdot m^{-3}$ for b2 and 32.4 $\mu g \cdot m^{-3}$ for b3). These clusters

318   passed over the ocean areas and accounted for more than half of all trajectories. The magnitude of total CC, IS and VE

319   exhibited a descending order from clusters b1 to b3. The dilution effects of clean ocean air masses played a vital role in

13

320   particulate pollution. In autumn (Fig 5c), there were the highest concentrations of PM$_{2.5}$ in cluster c1, with an average value

321   of 84.6 μg·m^{-3}. CC (23.1%) and IS (27.6%) contributed relatively highly in cluster c1, indicating that regional transport from

322   industrial regions might play an important role. For SIA, the proportion of NH$_4^+$ in these air masses was significantly higher

323   in autumn than those in other seasons (Table 2). As a tracer of the biomass burning source, the increase in the proportion of

324   NH$_4^+$ indicated that air pollution masses were heavily affected by nearby agricultural activities. In winter (Fig 7d), clusters

325   d1 (108.3 μg·m^{-3}) and d3 (122.6 μg·m^{-3}) originated from Shandong Province and the BTH, accounting for more than three-

326   quarters of the air masses. These air masses, which moved at high altitudes with a slow speed, could have carried abundant

327   air pollutants. Cluster d2 (153.9 μg·m^{-3}) was short-distance transport and derived from Jiangsu Province. The contribution of

328   SIA exhibited a descending order from clusters d1 (22.9%) to d3 (43.4%) to d2 (55.5%), corresponding to the transition from

329   long-range transport air masses to short-distance transport air masses.

330   Figure 6 shows the spatial distribution of the contribution from each source of PM$_{2.5}$ by the CWT method and

331   highlighted the potential geographic origins. For SIA (Fig. 6a), the high levels (10-15 μg·m^{-3}) of this source mainly

332   originated from local emissions in Jiangsu and regional transport from Shandong Province. For CC (Fig. 6b), the high

333   emissions (10-11 μg·m^{-3}) were distributed in the YRD and central China. The weighted concentration values of CC were

334   lower than those of the SIA. High concentrations near the center area are associated with local sources, while those far away

335   from the center area are indicative of regional transport (Shu et al., 2017). The secondary aerosol source was probably from

336   the accumulation of precursors emitted by local emissions. For IS and VE (Fig. 6c and d), there were no high potential areas

337   for these sources. The moderate weighted concentration values of IS (8-9 μg·m^{-3}) were potentially located in the north of

338   Jiangsu, Anhui, and Jiangxi, which were the most important industrial base in China. However, the industrial pollution

339   derived from long-range transport was attenuated by meteorological conditions (Table 2). In addition, after the

340   implementation of relevant control policies, many factories in the YRD were shut down and backward capacities in heavy

341   industries were cut down (Zheng et al., 2019). The potential source regions identified after the source weighting could better

342   reflect the spatial variations of source contribution.
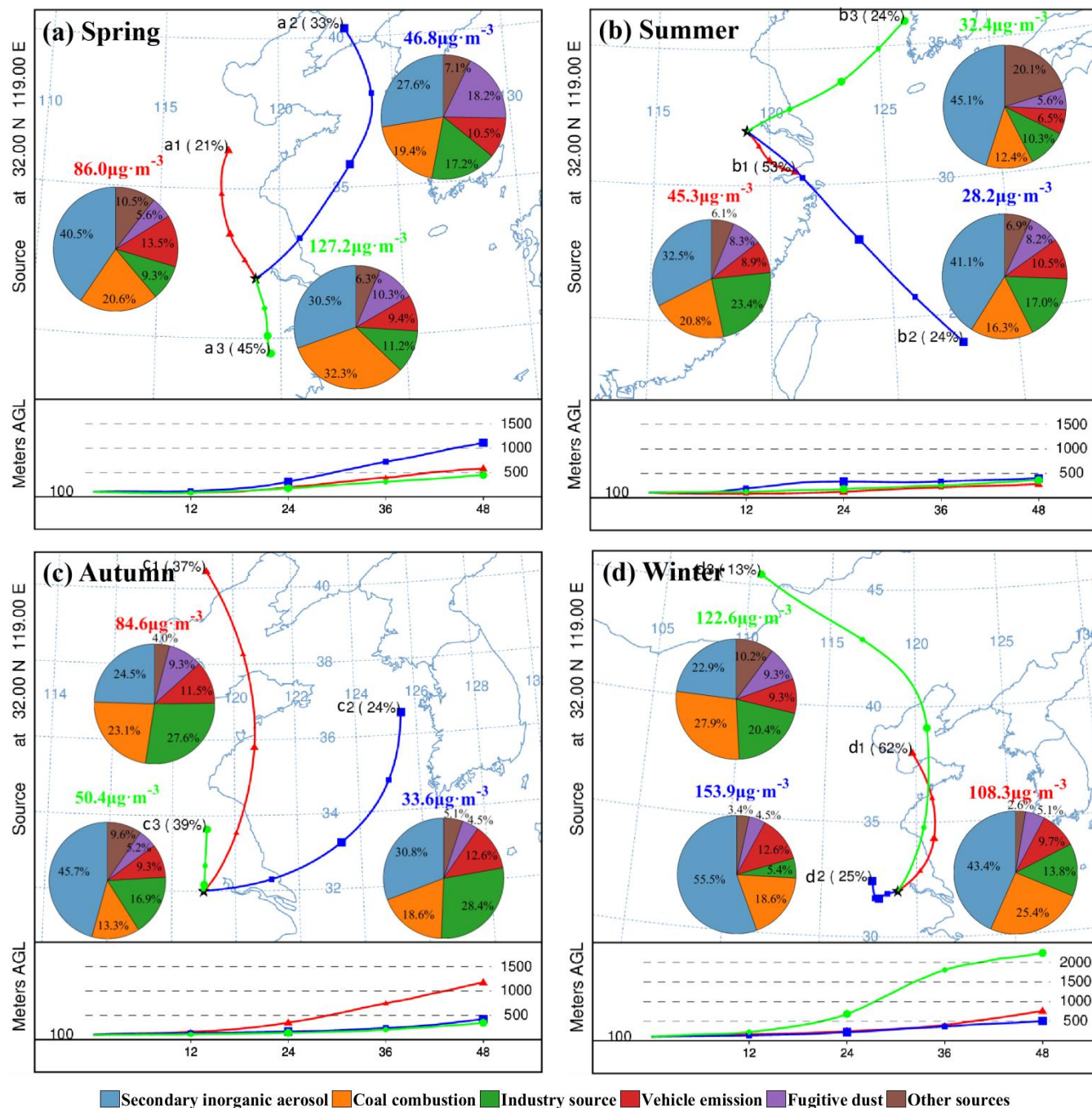
Figure 5. Source contributions to PM$_{2.5}$ grouped by air masses associated with different 48-h backward trajectory clusters. The pie charts show the source contributions for corresponding clusters.
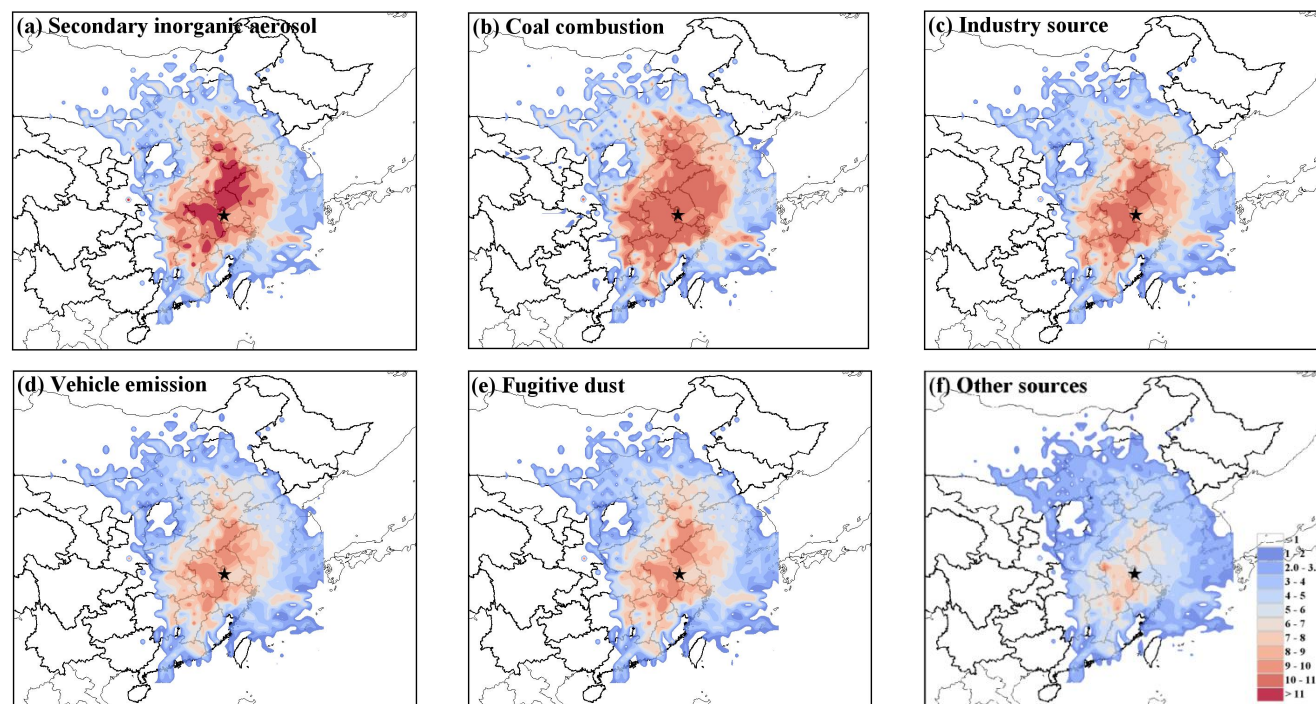
Figure 6. Potential source regions for individual sources of PM$_{2.5}$ identified by the CWT method from March 2018 to February 2019.

3.4 Non-carcinogenic and carcinogenic health risks of toxic metal elements in each source of PM$_{2.5}$

Figure 7 shows the HQ values of non-carcinogenic and the LCR values of carcinogenic risks in PM$_{2.5}$ and their total health risk in each source. For non-carcinogenic risk (Fig. 7a), the order of the average HQ values was Mn(0.47) > Ni (0.32) > As (0.14) > Cr (0.04) > V (0.02). The HQ values of toxic elements were all less than one, which indicated that there was no significant non-carcinogenic risk. However, the summation of five HQ values was higher than one, indicating that the combined exposure to the pollutant class still had adverse effects. The carcinogenic risk (Fig. 7b) posed by Ni (2.3×10^{-7}) and Pb (6.8×10^{-8}) were lower than 1×10^{-6} and could be acceptable. The carcinogenic risk level of Cr (1.0×10^{-7}) and As (1.8×10^{-5}) were within the tolerance or acceptable level (1×10^{-6}-1×10^{-4}). Figures 7 c and d show the integrated assessment of the source apportionment in toxic elements. IS accounted for the largest proportion of the non-carcinogenic and carcinogenic risk, with the HQ of 0.83 and the LCR of 5.8×10^{-6}, respectively. Although the PMF results indicated that SIA had the highest contribution to PM$_{2.5}$ (Fig. 4), the health risk results showed that the health risks of toxic elements from IS and CC were much higher than those from SIA. Previous studies showed that coal combustion sources in Beijing, Shanxi, and Jinan had higher respiratory exposure health risks, while the fugitive dust source in Liaoning contained higher levels of Pb, As, and Co (Zeng et al., 2021). It was related to the differences in PM$_{2.5}$ pollution characteristics and source contributions in different cities. The ingestion exposure may result in the potential health risk from IS, CC, and VE. Based

16

362   on the implementation of energy conservation and emission reduction policies, the main source of pollution in Nanjing is

363   SIA at present, and the health risk has been alleviated. However, we should pay more attention to the health burden of

364   vehicle emissions, coal combustion, and industrial processes.
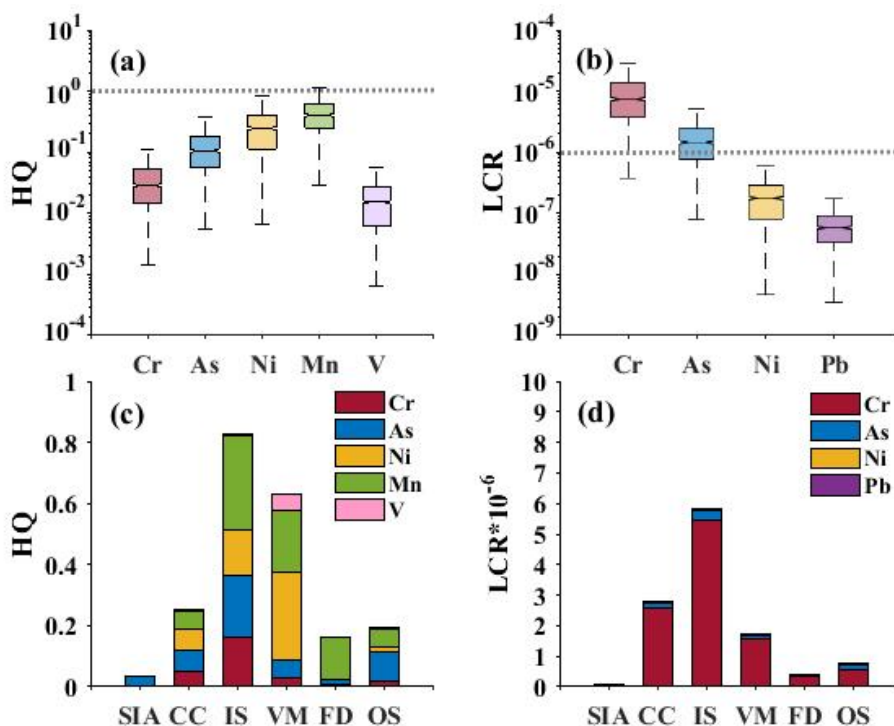
365   **Figure 7. Non-carcinogenic (a) and Carcinogenic (b) health risks of toxic elements and their total health risk (c and d) in each**

366   **source.**

3. Conclusions

368   Identifying and quantitatively assessing the contributions and health risks of pollution sources has played an important

369   role in formulating policies to control particle pollution. We have derived a high-quality $PM_{2.5}$ composition data set, based

370   on a chemical component monitoring from March 2018 to February 2019 in Nanjing. The PMF and back-trajectory results

371   were adopted to investigate the chemical characteristics and regional transports of each source. The health risk assessment

372   was used to explore non-carcinogenic and carcinogenic risks of toxic elements.

373   The results showed that $PM_{2.5}$ concentrations ranged from 6.7 to 234.0 $\mu g \cdot m^{-3}$, with an annual average of 68.7 $\mu g \cdot m^{-3}$.

374   Water-soluble ions contributed the most to $PM_{2.5}$. From summer to winter, the increase of NOR and SOR indicated that the

375   secondary transformation of gaseous pollutants was strongly positively correlated with RH. Based on values of NO_3^-/SO_4^{2-}

376   and OC/EC ratio, dominant vehicle emission occurred during the heavily polluted period, and the contribution of coal

377   combustion increased in winter. Based on the PMF model, the source variations and health risks were assessed. The

378   contribution of identified sources (including SIA (42.5%), CC (22.4%), IS (17.3%), VE (10.7%), FD (5.8%), and other

379   sources (1.3%)) had different spatial distributions and seasonal variations. The CWT analysis indicated that high emissions

380   (10-11 μg·m^{-3}) of SIA and CC were distributed in the YRD and central China in winter. Moderate emissions (8-9 μg·m^{-3}) of

381   IS and VE were potentially located in the north of Jiangsu, Anhui, and Jiangxi. PM$_{2.5}$ pollution from long-range transport

382   was attenuated by meteorological conditions. The carcinogenic and non-carcinogenic risks of toxic elements (Cr, As, Ni, Mn,

383   V, and Pb) mainly came from IS, VE, and CC, which were within the tolerance or acceptable level. Based on the

384   implementation of energy conservation and emission reduction policies, the main source of pollution in Nanjing is SIA at

385   present, and the health risk has been alleviated. However, we should pay more attention to the health burden of vehicle

386   emissions, coal combustion, and industrial processes.

387   This study provided new insight for PM$_{2.5}$ research between the source apportionment and health risk. The results

388   presented characteristics of chemical components, pinpointed secondary transformation processes leading to the high PM$_{2.5}$

389   concentrations, revealed spatial variations of source contribution, and provided new references for mega-cities to conduct

390   health risk analysis on air pollution control measures.

391   *Data Availability.*

392   Air quality monitoring data were acquired from the official NEMC real-time publishing platform

393   (https://air.cnemc.cn:18007/, last access: 7 April 2023). Meteorological data were obtained from the University of Wyoming

394   website (http://weather.uwyo.edu/, last access: 7 April 2023). The NCEP FNL data were taken from the NCEP

395   (https://rda.ucar.edu/datasets/, last access: 7 April 2023). These data can be downloaded for free as long as one agrees to the

396   official instructions.

397   *Author contributions.*

398   YZ and MX had the original ideas, designed the research, collected the data, and prepared the original draft. YZ, YL, and RZ

399   performed PMF experiments and carried out the data analysis. MX acquired financial support for the project leading to this

400   publication. TW, SL, BZ, and ML reviewed the initial draft and checked the English of the original paper.

406   *Competing interests.*

407   The contact author has declared that neither they nor their co-author has any competing interests.

References

412 Behrooz, R. D., Kaskaoutis, D. G., Grivas, G., and Mihalopoulos, N.: Human health risk assessment for toxic elements in the

413   extreme ambient dust conditions observed in Sistan, Iran, Chemosphere, 262,

414   https://doi.org/10.1016/j.chemosphere.2020.127835, 2021.

415 Brokamp, C., Jandarov, R., Rao, M. B., LeMasters, G., and Ryan, P.: Exposure assessment models for elemental components

416   of particulate matter in an urban environment: A comparison of regression and random forest approaches, Atmos.

417   Environ., 151, 1-11, https://doi.org/10.1016/j.atmosenv.2016.11.066, 2017.

418 Chen, D., Cui, H. F., Zhao, Y., Yin, L. N., Lu, Y., and Wang, Q. G.: A two-year study of carbonaceous aerosols in ambient

419     $PM_{2.5}$ at a regional background site for western Yangtze River Delta, China, Atmos. Res., 183, 351-361,

420   https://doi.org/10.1016/j.atmosres.2016.09.004, 2017.

421 Chen, Z. Y., Xie, X. M., Cai, J., Chen, D. L., Gao, B. B., He, B., Cheng, N. L., and Xu, B.: Understanding meteorological

422   influences on PM2.5 concentrations across China: a temporal and spatial perspective, Atmos. Chem. Phys., 18, 5343-5358,

423   https://doi.org/10.5194/acp-18-5343-2018, 2018.

424 Chow, W. S., Huang, X. H. H., Leung, K. F., Huang, L., Wu, X. R., and Yu, J. Z.: Molecular and elemental marker-based

425   source apportionment of fine particulate matter at six sites in Hong Kong, China, Sci. Total Environ., 813,

426   https://doi.org/10.1016/j.scitotenv.2021.152652, 2022.

427 Fan, H., Zhao, C. F., and Yang, Y. K.: A comprehensive analysis of the spatio-temporal variation of urban air pollution in

428   China during 2014-2018, Atmos. Environ., 220, https://doi.org/10.1016/j.atmosenv.2019.117066, 2020.

429 Fang, B., Zeng, H., Zhang, L., Wang, H. W., Liu, J. J., Hao, K. L., Zheng, G. Y., Wang, M. M., Wang, Q., and Yang, W. Q.:

430   Toxic metals in outdoor/indoor airborne $PM_{2.5}$ in port city of Northern, China: Characteristics, sources, and personal

431   exposure risk assessment, Environ. Pollut., 279, https://doi.org/10.1016/j.envpol.2021.116937, 2021.

432 Feng, X. Y., Tian, Y. Z., Xue, Q. Q., Song, D. L., Huang, F. X., and Feng, Y. C.: Measurement report: Spatiotemporal and

433   policy-related variations of PM2.5 composition and sources during 2015-2019 at multiple sites in a Chinese megacity,

434   Atmos. Chem. Phys., 21, 16219-16235, https://doi.org/10.5194/acp-21-16219-2021, 2021.

435 Gao, D., Xie, M., Liu, J., Wang, T. J., Ma, C. Q., Bai, H. K., Chen, X., Li, M. M., Zhuang, B. L., and Li, S.: Ozone

436   variability induced by synoptic weather patterns in warm seasons of 2014-2018 over the Yangtze River Delta region,

437   China, Atmos. Chem. Phys., 21, 5847-5864, https://doi.org/10.5194/acp-21-5847-2021, 2021.

438 Guevara, M., Jorba, O., Soret, A., Petetin, H., Bowdalo, D., Serradell, K., Tena, C., van der Gon, H. D., Kuenen, J., Peuch, V.

439 H., and Garcia-Pando, C. P.: Time-resolved emission reductions for atmospheric chemistry modelling in Europe during

440 the COVID-19 lockdowns, Atmos. Chem. Phys., 21, 773-797, https://doi.org/10.5194/acp-21-773-2021, 2021.

441 Huang, X. J., Liu, Z. R., Liu, J. Y., Hu, B., Wen, T. X., Tang, G. Q., Zhang, J. K., Wu, F. K., Ji, D. S., Wang, L. L., and

442 Wang, Y. S.: Chemical characterization and source identification of PM$_{2.5}$ at multiple sites in the Beijing-Tianjin-Hebei

443 region, China, Atmos. Chem. Phys., 17, 12941-12962, https://doi.org/10.5194/acp-17-12941-2017, 2017.

444 Islam, M. R., Jayarathne, T., Simpson, I. J., Werden, B., Maben, J., Gilbert, A., Praveen, P. S., Adhikari, S., Panday, A. K.,

445 Rupakheti, M., Blake, D. R., Yokelson, R. J., DeCarlo, P. F., Keene, W. C., and Stone, E. A.: Ambient air quality in the

446 Kathmandu Valley, Nepal, during the pre-monsoon: concentrations and sources of particulate matter and trace gases,

447 Atmos. Chem. Phys., 20, 2927-2951, https://doi.org/10.5194/acp-20-2927-2020, 2020.

448 Jiang, N., Duan, S. G., Yu, X., Zhang, R. Q., and Wang, K.: Comparative major components and health risks of toxic

449 elements and polycyclic aromatic hydrocarbons of PM$_{2.5}$ in winter and summer in Zhengzhou: Based on three-year data,

450 Atmos. Res., 213, 173-184, https://doi.org/10.1016/j.atmosres.2018.06.008, 2018.

451 Khan, M. F., Latif, M. T., Saw, W. H., Amil, N., Nadzir, M. S. M., Sahani, M., Tahir, N. M., and Chung, J. X.: Fine

452 particulate matter in the tropical environment: monsoonal effects, source apportionment, and health risk assessment,

453 Atmos. Chem. Phys., 16, 597-617, https://doi.org/10.5194/acp-16-597-2016, 2016.

454 Kumari, P., and Toshniwal, D.: Impact of lockdown measures during COVID-19 on air quality- A case study of India, Int. J.

455 Environ. Health Res., 32, 503-510, https://doi.org/10.1080/09603123.2020.1778646, 2022.

456 Li, T. T., Li, J., Jiang, H. X., Chen, D. H., Zong, Z., Tian, C. G., and Zhang, G.: Source Apportionment of PM(2.5)in

457 Guangzhou Based on an Approach of Combining Positive Matrix Factorization with the Bayesian Mixing Model and

458 Radiocarbon, Atmos, 11, https://doi.org/10.3390/atmos11050512, 2020.

459 Li, X. Y., Cheng, T. H., Shi, S. Y., Guo, H., Wu, Y., Lei, M., Zuo, X., Wang, W. N., and Han, Z. Y.: Evaluating the impacts

460 of burning biomass on regional transport under various emission conditions, Sci. Total Environ., 793,

461 https://doi.org/10.1016/j.scitotenv.2021.148481, 2021.

462 Li, X., Yan, C. Q., Wang, C. Y., Ma, J. J., Li, W. X., Liu, J. Y., and Liu, Y.: PM2.5-bound elements in Hebei Province,

463 China: Pollution levels, source apportionment and health risks, Sci. Total Environ., 806,

464 https://doi.org/10.1016/j.scitotenv.2021.150440, 2022.

465 Liu, J., Wu, D., Fan, S. J., Mao, X., and Chen, H. Z.: A one-year, on-line, multi-site observational study on water-soluble

466 inorganic ions in PM$_{2.5}$ over the Pearl River Delta region, China, Sci. Total Environ., 601, 1720-1732,

467 https://doi.org/10.1016/j.scitotenv.2017.06.039, 2017.

468 Liu, Y. K., Yu, Y. P., Liu, M., Lu, M., Ge, R. R., Li, S. W., Liu, X. R., Dong, W. B., and Qadeer, A.: Characterization and

469 source identification of PM2.5-bound polycyclic aromatic hydrocarbons (PAHs) in different seasons from Shanghai,

470 China, Sci. Total Environ., 644, 725-735, https://doi.org/10.1016/j.scitotenv.2018.07.049, 2018.

471 Liu, M. X., Huang, X., Song, Y., Tang, J., Cao, J. J., Zhang, X. Y., Zhang, Q., Wang, S. X., Xu, T. T., Kang, L., Cai, X. H.,
472   Zhang, H. S., Yang, F. M., Wang, H. B., Yu, J. Z., Lau, A. K. H., He, L. Y., Huang, X. F., Duan, L., Ding, A. J., Xue, L.
473   K., Gao, J., Liu, B., and Zhu, T.: Ammonia emission control in China would mitigate haze pollution and nitrogen
474   deposition, but worsen acid rain, Proc. Natl. Acad. Sci. U. S. A., 116, 7760-7765,
475   https://doi.org/10.1073/pnas.1814880116, 2019.

476 Lv, Z. F., Wang, X. T., Deng, F. Y., Ying, Q., Archibald, A. T., Jones, R. L., Ding, Y., Cheng, Y., Fu, M. L., Liu, Y., Man,
477   H. Y., Xue, Z. G., He, K. B., Hao, J. M., and Liu, H. A.: Source-Receptor Relationship Revealed by the Halted Traffic and
478   Aggravated Haze in Beijing during the COVID-19 Lockdown, Environ. Sci. Technol., 54, 15660-15670,
479   https://doi.org/10.1021/acs.est.0c04941, 2020.

480 Lv, L. L., Wei, P., Hu, J. N., Chen, Y. J., and Shi, Y. P.: Source apportionment and regional transport of PM2.5 during haze
481   episodes in Beijing combined with multiple models, Atmos. Res., 266, https://doi.org/10.1016/j.atmosres.2021.105957,
482   2022.

483 Nie, D. Y., Chen, M. D., Wu, Y., Ge, X. L., Hu, J. L., Zhang, K., and Ge, P. X.: Characterization of Fine Particulate Matter
484   and Associated Health Burden in Nanjing, Int. J. Env. Res. Public Health, 15, https://doi.org/10.3390/ijerph15040602,
485   2018.

486 Paatero, P., and Tapper, U.: POSITIVE MATRIX FACTORIZATION - A NONNEGATIVE FACTOR MODEL WITH
487   OPTIMAL UTILIZATION OF ERROR-ESTIMATES OF DATA VALUES, Environmetrics, 5, 111-126,
488   https://doi.org/10.1002/env.3170050203, 1994.

489 Sharma, S., Zhang, M. Y., Anshika, Gao, J. S., Zhang, H. L., and Kota, S. H.: Effect of restricted emissions during COVID-
490   19 on air quality in India, Sci. Total Environ., 728, https://doi.org/10.1016/j.scitotenv.2020.138878, 2020.

491 Shu, L., Xie, M., Gao, D., Wang, T. J., Fang, D. X., Liu, Q., Huang, A. N., and Peng, L. W.: Regional severe particle
492   pollution and its association with synoptic weather patterns in the Yangtze River Delta region, China, Atmos. Chem. Phys.,
493   17, 12871-12891, https://doi.org/10.5194/acp-17-12871-2017, 2017.

494 Sulaymon, I. D., Zhang, Y. X., Hopke, P. K., Zhang, Y., Hua, J. X., and Mei, X. D.: COVID-19 pandemic in Wuhan:
495   Ambient air quality and the relationships between criteria air pollutants and meteorological variables before, during, and
496   after lockdown, Atmos. Res., 250, https://doi.org/10.1016/j.atmosres.2020.105362, 2021.

497 Sun, P., Nie, W., Wang, T. Y., Chi, X. G., Huang, X., Xu, Z., Zhu, C. J., Wang, L., Qi, X. M., Zhang, Q., and Ding, A. J.:
498   Impact of air transport and secondary formation on haze pollution in the Yangtze River Delta: In situ online observations
499   in Shanghai and Nanjing, Atmos. Environ., 225, https://doi.org/10.1016/j.atmosenv.2020.117350, 2020.

500 Taylor, A. A., Tsuji, J. S., Garry, M. R., McArdle, M. E., Goodfellow, W. L., Adams, W. J., and Menzie, C. A.: Critical
501   Review of Exposure and Effects: Implications for Setting Regulatory Health Criteria for Ingested Copper, Environ.
502   Manage., 65, 131-159, https://doi.org/10.1007/s00267-019-01234-y, 2020.

503 Tong, S. Y., Kong, L. D., Yang, K. J., Shen, J. D., Chen, L., Jin, S. Y., Wang, C., Sha, F., and Wang, L.: Characteristics of
504   air pollution episodes influenced by biomass burning pollution in Shanghai, China, Atmos. Environ., 238,
505   https://doi.org/10.1016/j.atmosenv.2020.117756, 2020.

506 Tseng, C. H., Tsuang, B. J., Chiang, C. J., Ku, K. C., Tseng, J. S., Yang, T. Y., Hsu, K. H., Chen, K. C., Yu, S. L., Lee, W.
507   C., Liu, T. W., Chan, C. C., and Chang, G. C.: The Relationship Between Air Pollution and Lung Cancer in Nonsmokers
508   in Taiwan, J. Thorac. Oncol., 14, 784-792, https://doi.org/10.1016/j.jtho.2018.12.033, 2019.

509 Wang, H. B., Tian, M., Chen, Y., Shi, G. M., Liu, Y., Yang, F. M., Zhang, L. M., Deng, L. Q., Yu, J., Peng, C., and Cao, X.
510   Y.: Seasonal characteristics, formation mechanisms and source origins of $PM_{2.5}$ in two megacities in Sichuan Basin, China,
511   Atmos. Chem. Phys., 18, 865-881, https://doi.org/10.5194/acp-18-865-2018, 2018.

512 Wang, S. S., Hu, G. R., Yan, Y., Wang, S., Yu, R. L., and Cui, J. Y.: Source apportionment of metal elements in $PM_{2.5}$ in a
513   coastal city in Southeast China: Combined Pb-Sr-Nd isotopes with PMF method, Atmos. Environ., 198, 302-312,
514   https://doi.org/10.1016/j.atmosenv.2018.10.056, 2019.

515 Wang, S. B., Ji, Y. Q., Zhao, J. B., Lin, Y., and Lin, Z.: Source apportionment and toxicity assessment of $PM_{2.5}$-bound PAHs
516   in a typical iron-steel industry city in northeast China by PMF-ILCR, Sci. Total Environ., 713,
517   https://doi.org/10.1016/j.scitotenv.2019.136428, 2020.

518 Win, M. S., Zeng, J. Y., Yao, C. H., Zhao, M. F., Xiu, G. L., Xie, T. T., Rao, L. F., Zhang, L. Y., Lu, H., Liu, X. C., Wang,
519   Q. Y., and Lu, S. N.: Sources of HULIS-C and its relationships with trace metals, ionic species in $PM_{2.5}$ in suburban
520   Shanghai during haze and non-haze days, JAtC, 77, 63-81, https://doi.org/10.1007/s10874-020-09404-7, 2020.

521 Wong, Y. K., Liu, K. M., Yeung, C., Leung, K. K. M., and Yu, J. Z.: Measurement report: Characterization and source
522   apportionment of coarse particulate matter in Hong Kong: insights into the constituents of unidentified mass and source
523   origins in a coastal city in southern China, Atmos. Chem. Phys., 22, 5017-5031, https://doi.org/10.5194/acp-22-5017-2022,
524   2022.

525 Wu, X., Cao, F., Haque, M., Fan, M. Y., Zhang, S. C., and Zhang, Y. L.: Molecular composition and source apportionment
526   of fine organic aerosols in Northeast China, Atmos. Environ., 239, https://doi.org/10.1016/j.atmosenv.2020.117722, 2020.

527 Xie, M., Liao, J. B., Wang, T. J., Zhu, K. G., Zhuang, B. L., Han, Y., Li, M. M., and Li, S.: Modeling of the anthropogenic
528   heat flux and its effect on regional meteorology and air quality over the Yangtze River Delta region, China, Atmos. Chem.
529   Phys., 16, 6071-6089, https://doi.org/10.5194/acp-16-6071-2016, 2016.

530 Xie, J. J., Yuan, C. G., Xie, J., Niu, X. D., and He, A. E.: PM2.5-bound potentially toxic elements (PTEs) fractions,
531   bioavailability and health risks before and after coal limiting, Ecotoxicol. Environ. Saf., 192,
532   https://doi.org/10.1016/j.ecoenv.2020.110249, 2020.

533 Xu, J. S., Liu, D., Wu, X. F., Vu, T., Zhang, Y. L., Fu, P. Q., Sun, Y. L., Xu, W. Q., Zheng, B., Harrison, R. M., and Shi, Z.
534   B.: Source apportionment of fine organic carbon at an urban site of Beijing using a chemical mass balance model, Atmos.
535   Chem. Phys., 21, 7321-7341, https://doi.org/10.5194/acp-21-7321-2021, 2021.

536 Yan, Y., Zheng, Q., Yu, R. L., Hu, G. R., Huang, H. B., Lin, C. Q., Cui, J. Y., and Yan, Y.: Characteristics and provenance
537   implications of rare earth elements and Sr-Nd isotopes in PM2.5 aerosols and PM2.5 fugitive dusts from an inland city of
538   southeastern China, Atmos. Environ., 220, https://doi.org/10.1016/j.atmosenv.2019.117069, 2020.

539 Yan, Y. C., Liu, Z. R., Gao, W., Li, J. Y., Zhang, X. H., Chai, W. H., Bai, J. H., Hu, B., and Wang, Y. S.: Physiochemistry
540   characteristics and sources of submicron aerosols at the background area of North China Plain: Implication of air pollution
541   control in heating season, Atmos. Res., 249, https://doi.org/10.1016/j.atmosres.2020.105291, 2021.

542 Zeng, Y. Y., Cao, Y. F., Qiao, X., Seyler, B. C., and Tang, Y.: Air pollution reduction in China: Recent success but great
543   challenge for the future, Sci. Total Environ., 663, 329-337, https://doi.org/10.1016/j.scitotenv.2019.01.262, 2019.

544 Zhan, Y. Z. H., Xie, M., Gao, D., Wang, T. J., Zhang, M., and An, F. X.: Characterization and source analysis of water-
545   soluble inorganic ionic species in PM2.5 during a wintertime particle pollution episode in Nanjing, China, Atmos. Res.,
546   262, https://doi.org/10.1016/j.atmosres.2021.105769, 2021.

547 Zhang, L. L., Wilson, J. P., MacDonald, B., Zhang, W. H., and Yu, T.: The changing $PM_{2.5}$ dynamics of global megacities
548   based on long-term remotely sensed observations, Environ. Int., 142, https://doi.org/10.1016/j.envint.2020.105862, 2020.

549 Zheng, H., Kong, S. F., Yan, Q., Wu, F. Q., Cheng, Y., Zheng, S. R., Wu, J., Yang, G. W., Zheng, M. M., Tang, L. L., Yin,
550   Y., Chen, K., Zhao, T. L., Liu, D. T., Li, S. L., Qi, S. H., Zhao, D. L., Zhang, T., Ruan, J. J., and Huang, M. Z.: The
551   impacts of pollution control measures on $PM_{2.5}$ reduction: Insights of chemical composition, source variation and health
552   risk, Atmos. Environ., 197, 103-117, https://doi.org/10.1016/j.atmosenv.2018.10.023, 2019.

553 Zhou, D. R., Li, B., Huang, X., Virkkula, A., Wu, H. S., Zhao, Q. Y., Zhang, J., Liu, Q., Li, L., Li, C. Y., Chen, F., Yuan, S.
554   Y., Qiao, Y. Z., Shen, G. F., and Ding, A. J.: The Impacts of Emission Control and Regional Transport on $PM_{2.5}$ Ions and
555   Carbon Components in Nanjing during the 2014 Nanjing Youth Olympic Games, Aerosol And Air Quality Research, 17,
556   730-740, https://doi.org/10.4209/aaqr.2016.03.0131, 2017.

557 Zhu, Y. J., Xie, J. G., Huang, F. M., and Cao, L. Q.: Association between short-term exposure to air pollution and COVID-
558   19 infection: Evidence from China, Sci. Total Environ., 727, https://doi.org/10.1016/j.scitotenv.2020.138704, 2020.

559 Zong, Z., Wang, X. P., Tian, C. G., Chen, Y. J., Qu, L., Ji, L., Zhi, G. R., Li, J., and Zhang, G.: Source apportionment of
560      $PM_{2.5}$ at a regional background site in North China using PMF linked with radiocarbon analysis: insight into the
561   contribution of biomass burning, Atmos. Chem. Phys., 16, 11249-11265, https://doi.org/10.5194/acp-16-11249-2016,
562   2016.

563 Zou, B. B., Huang, X. F., Zhang, B., Dai, J., Zeng, L. W., Feng, N., and He, L. Y.: Source apportionment of $PM_{2.5}$ pollution
564   in an industrial city in southern China, Atmos. Pollut. Res., 8, 1193-1202, https://doi.org/10.1016/j.apr.2017.05.001, 2017.